

Delay grid multiplexing: simple time-based multiplexing and readout method for silicon photomultipliers

This content has been downloaded from IOPscience. Please scroll down to see the full text.

2016 Phys. Med. Biol. 61 7113

(<http://iopscience.iop.org/0031-9155/61/19/7113>)

View [the table of contents for this issue](#), or go to the [journal homepage](#) for more

Download details:

IP Address: 147.46.96.131

This content was downloaded on 26/09/2016 at 02:32

Please note that [terms and conditions apply](#).

You may also be interested in:

[Investigation of analog charge multiplexing schemes for SiPM based PET block detectors](#)

Evan Downie, Xin Yang and Hao Peng

[Analog signal multiplexing for PSAPD-based PET detectors](#)

Frances W Y Lau, Arne Vandenbroucke, Paul D Reynolds et al.

[Performance characterization of compressed sensing positron emission tomography detectors and data acquisition system](#)

Chen-Ming Chang, Alexander M Grant, Brian J Lee et al.

[Electrical delay line multiplexing for pulsed mode radiation detectors](#)

Ruud Vinke, Jung Yeol Yeom and Craig S Levin

[Design and optimization of a high-resolution PET detector module for small-animal PET based on a 12 × 12 silicon photomultiplier array](#)

Junwei Du, Jeffrey P Schmall, Kun Di et al.

[Optimized light sharing for high-resolution TOF PET detector based on digital silicon photomultipliers](#)

R Marcinkowski, S España, R Van Holen et al.

Delay grid multiplexing: simple time-based multiplexing and readout method for silicon photomultipliers

Jun Yeon Won^{1,2}, Guen Bae Ko^{1,2} and Jae Sung Lee^{1,2,3,4}

¹ Department of Nuclear Medicine, Seoul National University College of Medicine, Seoul 03080, Korea

² Department of Biomedical Sciences, Seoul National University College of Medicine, Seoul 03080, Korea

³ Institute of Radiation Medicine, Medical Research Center, Seoul National University College of Medicine, Seoul 03080, Korea

E-mail: jaes@snu.ac.kr

Received 12 May 2016, revised 28 July 2016

Accepted for publication 16 August 2016

Published 19 September 2016



Abstract

In this paper, we propose a fully time-based multiplexing and readout method that uses the principle of the global positioning system. Time-based multiplexing allows simplifying the multiplexing circuits where the only innate traces that connect the signal pins of the silicon photomultiplier (SiPM) channels to the readout channels are used as the multiplexing circuit. Every SiPM channel is connected to the delay grid that consists of the traces on a printed circuit board, and the inherent transit times from each SiPM channel to the readout channels encode the position information uniquely. Thus, the position of each SiPM can be identified using the time difference of arrival (TDOA) measurements. The proposed multiplexing can also allow simplification of the readout circuit using the time-to-digital converter (TDC) implemented in a field-programmable gate array (FPGA), where the time-over-threshold (ToT) is used to extract the energy information after multiplexing. In order to verify the proposed multiplexing method, we built a positron emission tomography (PET) detector that consisted of an array of 4×4 LGSO crystals, each with a dimension of $3 \times 3 \times 20 \text{ mm}^3$, and one-to-one coupled SiPM channels. We first employed the waveform sampler as an initial study, and then replaced the waveform sampler with an FPGA-TDC to further simplify the readout circuits. The 16 crystals were clearly resolved using only the time information obtained from the four readout channels. The

⁴ Address to whom any correspondence should be addressed.

Department of Nuclear Medicine, Seoul National University College of Medicine, 103 Daehak-ro, Jongno-gu, Seoul 03080, Korea.

coincidence resolving times (CRTs) were 382 and 406 ps FWHM when using the waveform sampler and the FPGA-TDC, respectively. The proposed simple multiplexing and readout methods can be useful for time-of-flight (TOF) PET scanners.

Keywords: multiplexing, silicon photomultiplier (SiPM), time-based positioning, time difference of arrival (TDOA), time-of-flight (TOF), time-over-threshold (ToT), time-to-digital converter (TDC)

(Some figures may appear in colour only in the online journal)

1. Introduction

Silicon photomultiplier (SiPM) is a new semiconductor photosensor used in positron emission tomography (PET) that features high signal amplification gain, fast temporal response, magnetic insensitivity, and compact size (Lee and Hong 2010, Roncali and Cherry 2011). The timing performance of the scintillation detectors based on the latest SiPMs are comparable or superior to those based on the conventional photomultiplier tubes (PMTs) (Cates *et al* 2015, Nemallapudi *et al* 2015). In addition, the magnetic insensitivity and compact size of SiPMs allow for the simultaneous PET and magnetic resonance imaging (MRI) scans (Hong *et al* 2012, Yamamoto *et al* 2012, Yoon *et al* 2012, Olcott *et al* 2015, Wehrl *et al* 2015, Weissler *et al* 2015, Jung *et al* 2016, Ko *et al* 2016a, 2016b).

The compact size of SiPM also allows one-to-one coupling of the SiPM channel with the scintillation crystal element in the PET detector module, thus yielding the superior energy and timing performance of the PET detector by enhancing the collection efficiency of scintillation light emitted from the crystal (Kwon and Lee 2014). Furthermore, we can draw the best performance from the PET detector by individually reading the electrical signal from each SiPM that is one-to-one coupled with the scintillation crystal (Kim *et al* 2011, Yeom *et al* 2013a). However, this individual signal readout from SiPM is technically challenging at the system level implementation of PET scanners. Heat generated from the large volume of front-end and readout electronics required to manage the individual signals can degrade the SiPM characteristics if the PET detectors and the electronics are not properly cooled. In combined PET/MRI machines, there is a space constraint because the PET detectors and the electronics are usually placed between the radio-frequency coil and the gradient coil. The sophisticated application-specific integrated circuits (ASICs) can manage the signals from the individual SiPM channels with low power consumption and small space requirements (Anghinolfi *et al* 2004, Shimazoe *et al* 2010, Harion *et al* 2014). However, this approach has the disadvantages of relatively long development time and high developing cost.

The multiplexing of signals from multiple SiPM channels is an alternative method for managing the large number of output channels from the SiPM-based PET detectors. Because the multiplexing method is sub-optimal but less costly than the ASIC-based approach, it is used widely in the development of new PET detectors based on the SiPM arrays or the multi-channel PMTs. The most widely used multiplexing methods for the PET detectors are the charge division and the row/column sum readout methods. In the charge division methods, the number of readout channels is reduced to four or five (usually, four channels for encoding the position information and one channel for timing measurement) using resistor (Siegel *et al* 1996, Goertzen *et al* 2013, Ko *et al* 2013) or capacitor (Downie *et al* 2013, Olcott *et al* 2013) networks. The resistive charge division circuit coupled to the SiPM array has the high RC constant, and the rise time of its output signals are considerably discrepant depending on

the SiPM position of the resistor network, thus highly degrading the timing resolution of the PET detectors. The capacitive charge division circuit provides better temporal response than the resistive one. However, the signal distortion is the main disadvantage of the capacitive charge division and usually yields the negative impact on energy resolution. The row/column sum readout offers higher signal-to-noise ratio than the charge division methods, but requires a larger number of readout channels (Popov *et al* 2006, Kwon and Lee 2014, Stolin *et al* 2014). Moreover, both the charge division and the row/column sum readout methods usually demand the charge measurement devices, such as the analog-to-digital converters (ADCs), and a subsequent digital signal processor or a field-programmable gate array (FPGA). Time pickoff devices are also required for timing measurement.

The waveform sampling method that uses a fast waveform sampler provides both charge and timing information without the need of an additional time pickoff device (Ritt *et al* 2010). In addition, the time-based multiplexing method that uses a waveform sampler can simplify the multiplexing circuits because the passive components required for charge division can be removed (Kim *et al* 2012, 2015). However, the waveform sampler should contain the ADC and a subsequent FPGA, thus the readout circuit cannot be fully simplified.

In this paper, we propose a new fully time-based multiplexing and readout method that uses a delay grid and a time-to-digital converter (TDC) implemented in an FPGA. The position of each SiPM within a multiplexing circuit (delay grid) is decoded using the principle of time difference of arrival (TDOA) positioning, such as the global positioning system (GPS). Energy information is obtained using the time-over-threshold (ToT) technique after multiplexing thanks to minimal signal distortion by a delay grid circuit. The main advantage of the delay grid multiplexing combined with a time-based readout method is simplicity. In the multiplexing circuit, none of the active and passive components are used for encoding the position information. In the readout circuit, a single FPGA that embeds an in-house developed multi-channel TDC acquires the position, the timing, and the energy information without the requirement of an ADC.

2. Materials and methods

2.1. Position decoding principle

In the GPS that uses the TDOA positioning, the signal from the transmitter propagates through the medium and is received by multiple synchronized receivers. The position of the transmitter is localized using the known locations of the receivers and the TDOA information.

Similar to GPS, the position information on the fired SiPM can be decoded using the innate transit time differences from the SiPM channel to the readout channels. The transmitters, the medium, and the receivers in GPS correspond to the SiPM channels, the delay grid, and the time pickoff devices in the proposed multiplexing method. The delay grid consists of the traces in the row and column directions on a printed circuit board (PCB) where the SiPM channels of each row are connected and two column traces tie the ends of the row traces, as shown in figure 1. Unit delay (u) is the transit time between the adjacent cathodes. The four corner nodes of the delay grid, referred to as the A, B, C, and D nodes in a counterclockwise direction, are connected into the amplifiers and the output of each amplifier is fed into the time pickoff device. When the SiPMs fire, the current signals from the SiPM flow into the delay grid and the identical signals are fed into the four corner nodes with the difference in transit times. As indicated in table 1, the transit times from the SiPM channel to the readout channels are encoded uniquely. Using the TDOA measurements obtained at the A, B, C, and D nodes, the positions can be decoded as follows:

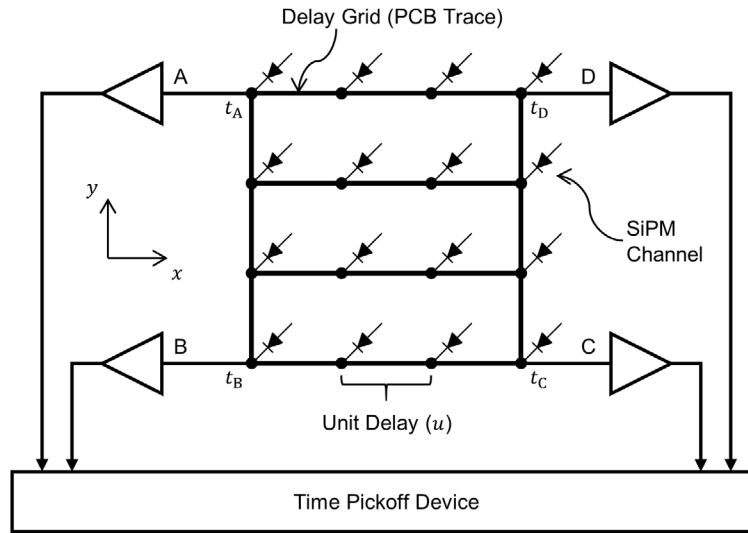


Figure 1. Conceptual diagram for the delay grid multiplexing. Position for each SiPM channel is uniquely encoded using the innate transit times from a SiPM channel to the four corner nodes.

Table 1. Look-up table for decoding the position and the time information.

Firing position		Corner node arrival time				Decoded position		Gamma arrival time
x	y	t_A	t_B	t_C	t_D	\hat{x}	\hat{y}	t_{ABCD}
0	0	$3u + t_\gamma$	$0u + t_\gamma$	$3u + t_\gamma$	$6u + t_\gamma$	$-1.5u$	$-1.5u$	$3u + t_\gamma$
0	1	$2u + t_\gamma$	$1u + t_\gamma$	$4u + t_\gamma$	$5u + t_\gamma$	$-1.5u$	$-0.5u$	
0	2	$1u + t_\gamma$	$2u + t_\gamma$	$5u + t_\gamma$	$4u + t_\gamma$	$-1.5u$	$0.5u$	
0	3	$0u + t_\gamma$	$3u + t_\gamma$	$6u + t_\gamma$	$3u + t_\gamma$	$-1.5u$	$1.5u$	
1	0	$4u + t_\gamma$	$1u + t_\gamma$	$2u + t_\gamma$	$5u + t_\gamma$	$-0.5u$	$-1.5u$	
1	1	$3u + t_\gamma$	$2u + t_\gamma$	$3u + t_\gamma$	$4u + t_\gamma$	$-0.5u$	$-0.5u$	
\vdots	\vdots	\vdots	\vdots	\vdots	\vdots	\vdots	\vdots	
3	3	$3u + t_\gamma$	$6u + t_\gamma$	$3u + t_\gamma$	$0u + t_\gamma$	$1.5u$	$1.5u$	

$$\hat{x} = ((t_A - t_D) + (t_B - t_C))/4. \tag{1}$$

$$\hat{y} = ((t_B - t_A) + (t_C - t_D))/4. \tag{2}$$

In equations (1) and (2), \hat{x} and \hat{y} are decoded positions. The values t_A , t_B , t_C , and t_D are the corner node arrival times at the A, B, C, and D nodes, which are the sums of the transit times from the SiPM channel to the A, B, C, and D nodes and the gamma arrival time (t_γ), respectively. The t_γ is the time when the gamma ray interacts with the SiPM-based scintillation detector. The denominator of four in these equations is the normalization factor.

2.2. Detector for concept verification of delay grid multiplexing

Figure 2 shows a SiPM-based detector assembled to show the feasibility of the proposed multiplexing method. The SiPM detector consisted of an array of 4×4 lutetium

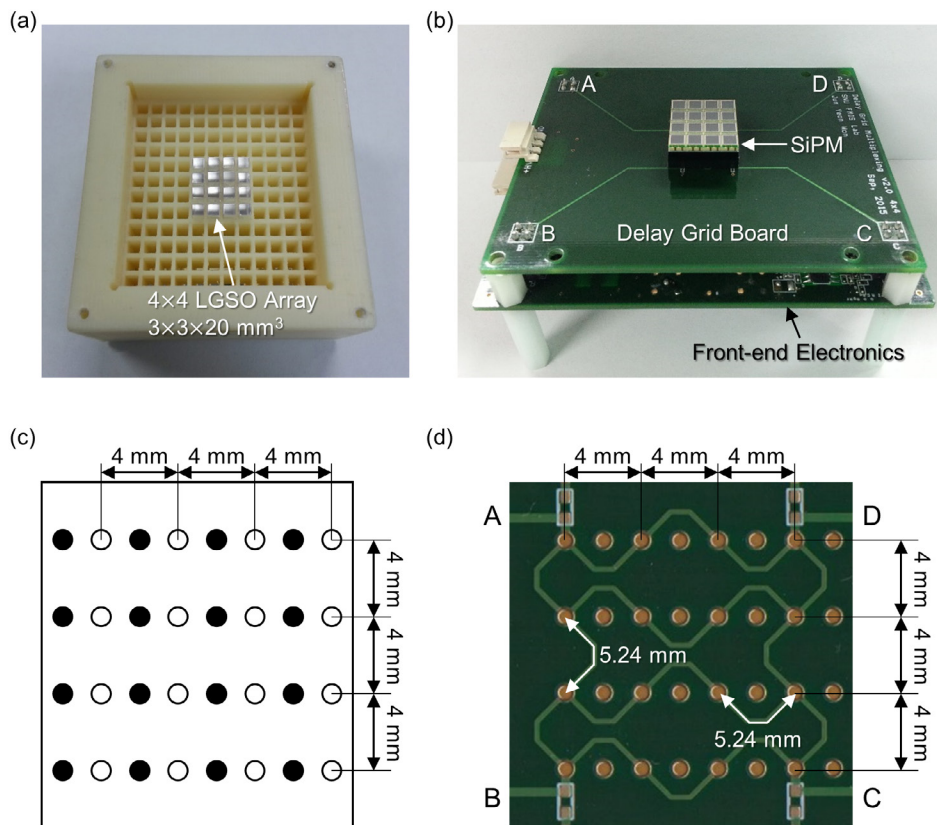


Figure 2. LGSO/SiPM detector using the proposed multiplexing method. (a) LGSO crystal array assembled into the frame. (b) Mounted SiPM on a delay grid board and the front-end electronics. (c) Backside of the employed SiPM. The blank and the filled circles indicate the pinout of the cathodes and the anodes, respectively. (d) Detailed view of a delay grid board.

gadolinium oxyorthosilicate (LGSO, $\text{Lu}_{1.9}\text{Gd}_{0.1}\text{SiO}_4\text{:Ce}$; Hitachi Chemical, Japan) crystals and one-to-one coupled SiPM (S11064-050P; Hamamatsu Photonics, K.K., Japan) as shown in figures 2(a) and (b). Each SiPM channel had an active area of $3 \times 3 \text{ mm}^2$ and both pitches of the cathode pins along the x and y directions were 4 mm as shown in figure 2(c). Each crystal had a dimension of $3 \times 3 \times 20 \text{ mm}^3$. All crystal surfaces were chemically polished and wrapped with enhanced specular reflectors (ESR; 3M, MN), with the exception of the exit face. Optical adhesive (Optically Clear Adhesive 8146-4; 3M, MN) with a refractive index of 1.474 and a uniform thickness of $100 \mu\text{m}$ was used to improve the optical coupling between the crystal and the SiPM.

All the crystals were assembled into an in-house frame produced in our previous work (Kwon and Lee 2014) using a 3D printer (Mojo; Stratasys, MN), as shown in figure 2(a). The crystal pitches along the x and y directions were 4.05 and 4.50 mm, respectively, which were equal to the SiPM pitches. As shown in figure 2(b), the LGSO/SiPM detector was mounted on a delay grid board.

The delay grid is a planar array of the microstrips on a flame retardant-4 (FR-4) substrate with the relative permittivity of 4.3 as shown in figure 2(d). The trace lengths between the

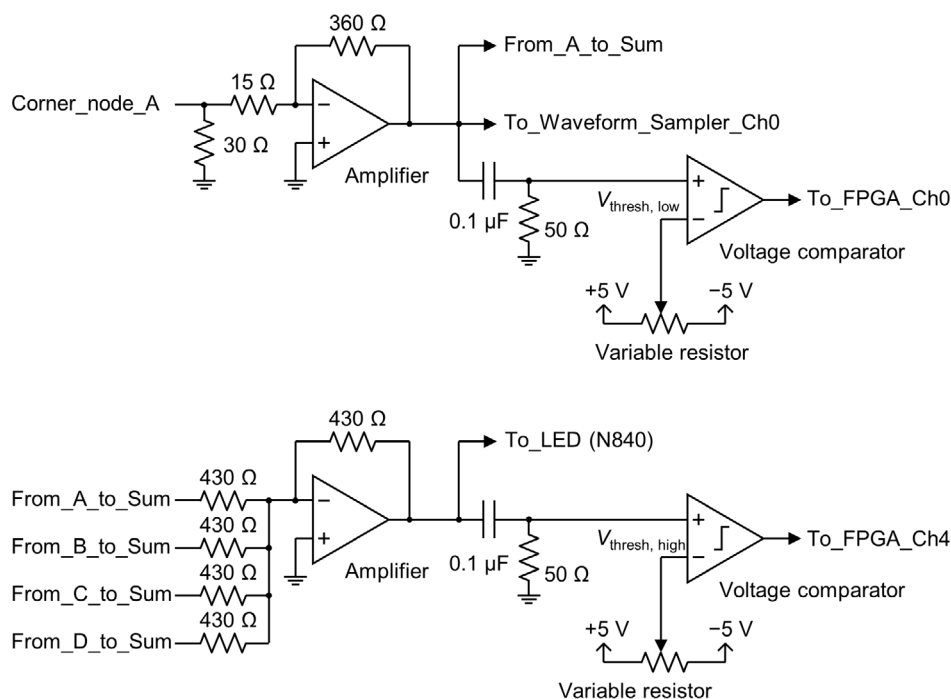


Figure 3. Schematic of the front-end electronics for the LGSO/SiPM detector. In the measurements using the waveform sampler, the bypass capacitors between the amplifiers and the comparators were detached. In the measurements using the FPGA-TDC, the cables connecting the front-end electronics to the waveform sampler and the leading edge discriminator (LED) module were detached.

cathode pins along the x and y directions were 5.24 mm. The width of the trace and the height with respect to the reference plane were 0.3 and 1.3 mm, respectively.

2.3. Front-end electronics

Front-end electronics provided either analog or digital signals containing the corner node arrival times with the time pickoff device. The signal chain was as follows. The four corner nodes of the delay grid board were connected to an in-house front-end electronics that contained the amplifiers and the comparators, as shown in figure 2(b).

Figure 3 shows the detailed schematic of the front-end electronics for the LGSO/SiPM detector. The current signals that arrived at the A, B, C, and D nodes were converted into the voltage signals with input impedance of $10\ \Omega$ and then amplified by -24 using inverting amplifiers. These signals were denoted as the A, B, C, and D signals, respectively. The summing amplifier added the A, B, C, and D signals and then provided the Sum signal. The traces from the A, B, C, and D amplifiers to the summing amplifier were designed to be the same lengths. Either analog A, B, C, and D signals or digital A, B, C, D, and Sum signals after discriminating the analog signals with the comparators were transmitted to the time pickoff device. The voltage threshold of the comparator was adjusted using a variable resistor and fixed during the measurement.

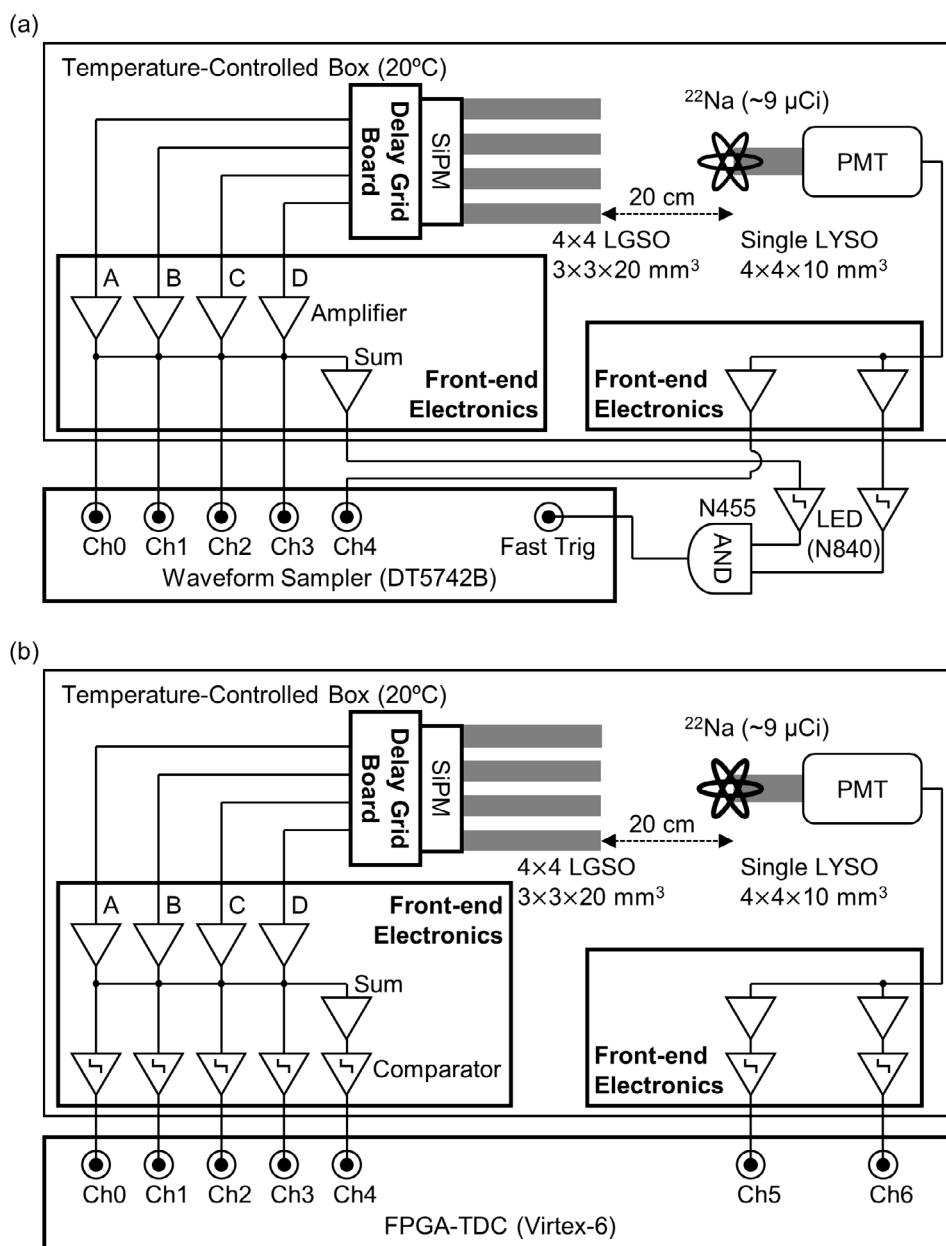


Figure 4. (a) Experimental setup using the waveform sampler. (b) Experimental setup using the FPGA-TDC.

2.4. Data acquisition setup

The LGSO/SiPM detector was evaluated in the coincidence detection mode with a reference detector, as shown in figure 4. We used the PMT-based scintillation detector with single timing resolution (STR) of 197 ps full width at half maximum (FWHM) as the reference detector (Ito *et al* 2013). A ^{22}Na point source (approximately 9 μCi) was attached to the reference

detector. The distance between the LGSO/SiPM and reference detectors was 20 cm. The ambient temperature was fixed at 20 °C using a temperature-controlled box.

We obtained 400 000 coincidence events for every measurement, with the exception of ToT nonlinearity calibration. In order to calibrate the nonlinearity of ToT, we acquired 1024 000 coincidence events for a ^{22}Na and 1024 000 singles events for ^{131}I and ^{137}Cs .

2.4.1. Data acquisition using the waveform sampler. For the purpose of initial verification, we used a fast waveform sampler (DT5742B; CAEN, Italy) based on switched capacitor arrays (SCAs). The SCA is the fourth version of the domino ring sampler (DRS4; PSI, Switzerland) and provides a resolution of 12 bits and a sampling rate of up to 5 Giga-samples s^{-1} (Ritt *et al* 2010).

The leading edge discriminator (LED) modules (N840; CAEN, Italy) and a coincidence unit (N455; CAEN, Italy) were used to obtain only coincidence events, as shown in figure 4(a). The A, B, C, and D signals were acquired using a waveform sampler at the respective readout channels. The output of the summing amplifier was used to generate a trigger, and instead, the Sum signal was obtained by adding the sampled A, B, C, and D waveforms. The time differences from the four corner nodes to the respective readout channels due to cable length differences were corrected before adding the sampled A, B, C, and D waveforms. The signal from the reference detector was also sampled.

The common bias voltage was applied to all SiPM channels where the breakdown voltages were -69.7V . The overvoltage was swept from 2.1 to 3.6 V (bias voltages from -71.8 to -73.3V) in steps of 0.3 V to find the optimal bias voltage where the SiPM provided the lowest coincidence resolving time (CRT).

2.4.2. Data acquisition using the FPGA-TDC. After verifying the concept of delay grid multiplexing using the waveform sampler, we replaced the waveform sampler with an FPGA-TDC to verify that the readout circuits can be further simplified. A multi-channel TDC with a 10 ps resolution and the sub-10 ps single-shot precision implemented in a Virtex-6 FPGA (ML605; Xilinx, San Jose, CA) was used (Won and Lee 2016, Won *et al* 2016).

In the front-end electronics for the LGSO/SiPM detector, the A, B, C, D, and Sum signals of the LGSO/SiPM detector were discriminated using the comparators that served as the LEDs, and then the digital signals that contained the arrival times and ToT were transmitted to the FPGA-TDC. In the front-end electronics for the reference detector, the signal from the reference detector was discriminated by two comparators with different threshold levels. The details on the dual-threshold ToT is discussed in section 2.5.2.1. In the FPGA, either singles or coincidence events within the predetermined time window were obtained (Ko *et al* 2011). The overvoltage of 2.7 V at which the SiPM provided the lowest CRT in the measurements using the waveform sampler was applied to the LGSO/SiPM detector when the FPGA-TDC was employed as a data acquisition system.

2.5. Data processing and analysis

2.5.1. Waveform sampler.

2.5.1.1. Rise time and decay time. To show that the signal was not distorted by the multiplexing circuit, the rise and decay times of the A, B, C, D, and Sum signals were obtained. The rise time was evaluated using the time taken by a signal to change from 10% to 90% of its peak amplitude (V_{max}). The decay time (τ) was obtained by fitting the trailing edge of the waveform to an exponential decay function $V_{\text{max}} \times \exp(-t/\tau)$.

2.5.1.2. Time pickoff. To obtain the position and the gamma arrival time (t_γ), we sampled the signals at 5 Giga-samples s^{-1} and interpolated the leading edge of the waveform using a cubic spline interpolation by a factor of 20 to obtain the resolution of 10 ps, and thus minimize the quantization error. We picked off the corner node arrival times by applying either constant voltage discriminator (also known as LED) or constant fraction discriminator (CFD) to the leading edge of the interpolated waveforms where the baseline for time pickoff was determined at the onset of the signal with time window of 2 ns in order to minimize the effect of dark noise on time pickoff (Schaart *et al* 2010, Yeom *et al* 2013b). The threshold for time pickoff was determined as the percentage of peak amplitude of events within an energy window and denoted as the percentage (%) threshold hereinafter. For LED, the constant voltage threshold calculated by averaging the percentage thresholds of all the events within the energy window was applied to every signal. For CFD, the threshold was determined as a constant percentage of peak amplitude for each signal.

2.5.1.3. Position. The position information was obtained from the corner node arrival times t_A , t_B , t_C , and t_D using equations (1) and (2). Both LED and CFD were employed and the percentage threshold used for obtaining the position information was swept from 2% to 40% in order to analyze the effect of threshold on the position.

The flood map was used to display the position information, while the events within a 400–600 keV energy window were employed. Flood-map quality was evaluated using a distance-to-width ratio (DWR) in the flood map (Ko and Lee 2015), also known as the k -parameter (Du *et al* 2013, Lee and Lee 2015). The DWR is defined as the distance between the two adjacent spots in the flood map to the average FWHM of the two spots, and it is calculated as follows:

$$\text{DWR} = \frac{1}{N_{\text{adj}}} \left(\sum_{i,j \in (\text{adj pair})}^{N_{\text{adj}}} \left(\frac{x_i - x_j}{(w_{x,i} + w_{x,j})/2} + \frac{y_i - y_j}{(w_{y,i} + w_{y,j})/2} \right) \right). \quad (3)$$

In equation (3), x_i , y_i and x_j , y_j are the x and y positions of the i th and j th crystals in the flood map, respectively. $w_{x,i}$, $w_{y,i}$ and $w_{x,j}$, $w_{y,j}$ are the FWHM of 1D profiles along the x and y directions of the i th and j th crystals, respectively. N_{adj} is the number of adjacent crystal pairs. A larger DWR indicates that the crystals are more clearly resolved.

To perform a per-crystal analysis, the crystals in the flood map were identified using the k -means clustering, while the initial values of the iterations were determined as the peak positions of the flood map. All the data were represented as the mean \pm standard deviation of the measurements of resolved crystals.

2.5.1.4. Energy. Energy information was calculated using the integration of sampled waveforms (sum of areas of the baseline-corrected A, B, C, and D waveforms). The baseline for energy integration was calculated using the mean value of the first 50 data points (10 ns) before the onset of the signal on an event-by-event basis. The energy integration window was 700 data points (140 ns).

The gain uniformity and the energy resolution were evaluated. The gain uniformity of the LGSO/SiPM detector was evaluated using the normalized gain, which was obtained by normalizing the photopeak positions of the energy spectra for the photopeak position of the detector channel with the highest gain to be 100%. The energy resolution was obtained by fitting the energy with a Gaussian function on a per-crystal basis.

2.5.1.5. CRT. The value t_γ can be calculated using the average value (t_{ABCD}) of t_A , t_B , t_C , and t_D as indicated in table 1 and equation (4).

$$t_{\text{ABCD}} = (t_{\text{A}} + t_{\text{B}} + t_{\text{C}} + t_{\text{D}})/4. \quad (4)$$

In addition, t_{γ} can be obtained using the conventional method that discriminates the Sum signal. The Sum signal can be generated either using the summing amplifier (Goertzen *et al* 2013, Ko *et al* 2013, Stolin *et al* 2014) or adding the sampled A, B, C, and D waveforms (Olcott *et al* 2013). This arrival time, acquired by applying LED or CFD to the Sum signal, is referred to as t_{Sum} . Thus, t_{γ} can be acquired using four time pickoff methods by regarding either t_{ABCD} or t_{Sum} as t_{γ} and using either LED or CFD. We represent the time pickoff methods using the notations of $\{t_{\text{ABCD}}, \text{LED}\}$, $\{t_{\text{ABCD}}, \text{CFD}\}$, $\{t_{\text{Sum}}, \text{LED}\}$, and $\{t_{\text{Sum}}, \text{CFD}\}$. The percentage threshold used to pickoff t_{γ} was swept from 1% to 5% in steps of 0.5% and the 2% threshold yielded the lowest CRT values for four time pickoff methods, and thus the 2% threshold was employed.

The events within the 400–600 keV energy windows of the LGSO/SiPM and reference detectors were employed to evaluate the CRT. The CRT between two identical LGSO/SiPM detectors ($\text{CRT}_{\text{SiPM/SiPM}}$) was calculated and notated hereinafter. From the FWHM of Gaussian fits applied to the time-difference spectra between the LGSO/SiPM and reference detectors ($\text{FWHM}_{\text{SiPM/PMT}}$), The STR of the reference detector of 197 ps FWHM (STR_{PMT}) was subtracted in the quadrature, and then that of the LGSO/SiPM detector was multiplied by $\sqrt{2}$ (Ito *et al* 2013), as indicated in equation (5).

$$\text{CRT}_{\text{SiPM/SiPM}} = \sqrt{2} \times \sqrt{\text{FWHM}_{\text{SiPM/PMT}}^2 - \text{STR}_{\text{PMT}}^2}. \quad (5)$$

2.5.2. FPGA-TDC.

2.5.2.1. Dual-threshold ToT. Dual-threshold ToT was employed for both the LGSO/SiPM and reference detectors to extract the precise timing and energy information. As shown in figure 5, the arrival time (t_{Arrival}) was obtained using the time when the signal crossed the low threshold ($V_{\text{thresh,low}}$) in its leading edge, while the ToT was calculated by subtracting this arrival time from the time when the signal crossed the high threshold ($V_{\text{thresh,high}}$) in its trailing edge. For the LGSO/SiPM detector, the $V_{\text{thresh,low}}$ of 2% threshold and the $V_{\text{thresh,high}}$ of 40% threshold were applied to the four corner readout channels and Sum readout channel, respectively; the ToT was calculated within an FPGA by subtracting t_{ABCD} from the time when the Sum signal crossed the $V_{\text{thresh,high}}$ in its trailing edge. For the reference detector, the $V_{\text{thresh,low}}$ of 5% threshold and the $V_{\text{thresh,high}}$ of 30% threshold were applied to the respective channels. For both detectors, false events with peak amplitudes lower than the $V_{\text{thresh,high}}$ were rejected.

The ToT measurement was calibrated into the energy value using the calibration curve that compensated both nonlinearities of SiPM and ToT (Grant and Levin 2014).

$$\text{ToT}(E) = c + a \times \ln[1 - \exp(-b \times E)]. \quad (6)$$

In equation (6), E indicates the energy of the incident gamma ray and a , b , and c are the constants to be determined for each crystal. Nonlinearity calibration was conducted in three steps. First, we obtained the photopeak positions of the ToT spectra for three radioisotopes with known energies: ^{131}I (364 keV), ^{22}Na (511 keV), and ^{137}Cs (662 keV). Second, we solved equation (6) to acquire the calibration curve on a per-crystal basis. Third, we applied per-crystal calibration curves to the ToT measurements.

2.5.2.2. Performance evaluation. The x and y positions and the gamma arrival time were calculated from the corner node arrival times obtained by an FPGA-TDC using the equations (1), (2) and (4), respectively. Energy, DWR, and CRT were assessed using the same data analysis procedures conducted with the waveform sampler.

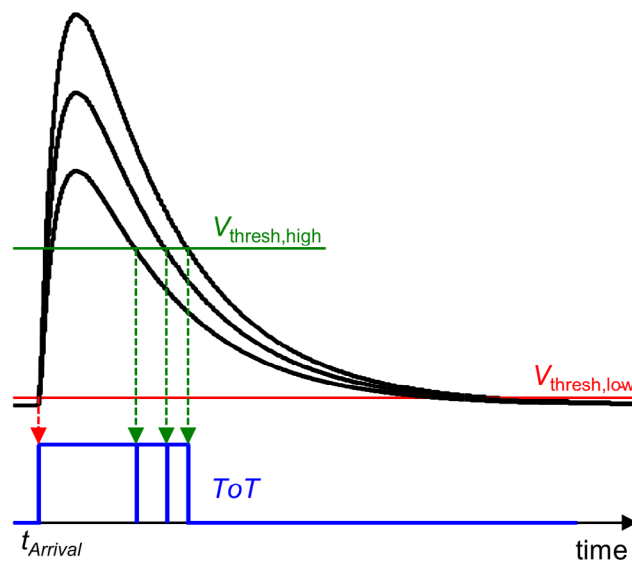


Figure 5. Conceptual diagram for the dual-threshold ToT.

3. Results

3.1. Waveform sampler

3.1.1. Waveform, rise time, and decay time. Figure 6 shows the A, B, C, and D signals that originated from the corner, edge, and center locations of the multiplexing circuit. For each event, the A, B, C, and D signals were almost identical, but with the TDOAs. The TDOAs described in table 1 were measured as expected. The signal arrived at the four corner nodes in order of closeness from the firing SiPM channel to the corner nodes. As shown in figure 6(b), the signal that originated from the SiPM channel location (1, 3) arrived at the A, D, B, and C nodes in order.

We could observe that the signal shape and the amplitude did not change considerably as the signal propagated along the delay grid. Although there were slight differences at the onsets of the A, B, C, and D signals, the overall signal shapes, including rise and decay times, were consistent throughout the multiplexed SiPM channels. Figures 7 and 8 show the average rise and decay times of the A, B, C, D, and Sum signals corresponding to photopeak events detected at 16 SiPM channels, respectively. The rise times of the A, B, C, D, and Sum signals were 19.0 ± 0.3 , 19.0 ± 0.4 , 18.5 ± 0.3 , 18.9 ± 0.2 , and 19.0 ± 0.2 ns, respectively. The decay times of the A, B, C, D, and Sum signals were 125 ± 4 , 125 ± 4 , 127 ± 2 , 127 ± 1 , and 126 ± 1 ns, respectively. The rise and decay times of the A, B, C, and D signals were almost the same and also uniform throughout 16 SiPM channels. In addition, the rise and decay times of the Sum signal were more consistent than those of the A, B, C, and D signals.

3.1.2. Flood map. Figure 9 shows the flood maps acquired using LED and CFD methods for the overvoltages of 2.1 V–3.6 V and the percentage thresholds of 2%–40%. The 16 crystals were clearly resolved for all measurements. In addition, as the percentage threshold increased, the size of the flood map also increased and a pincushion distortion appeared.

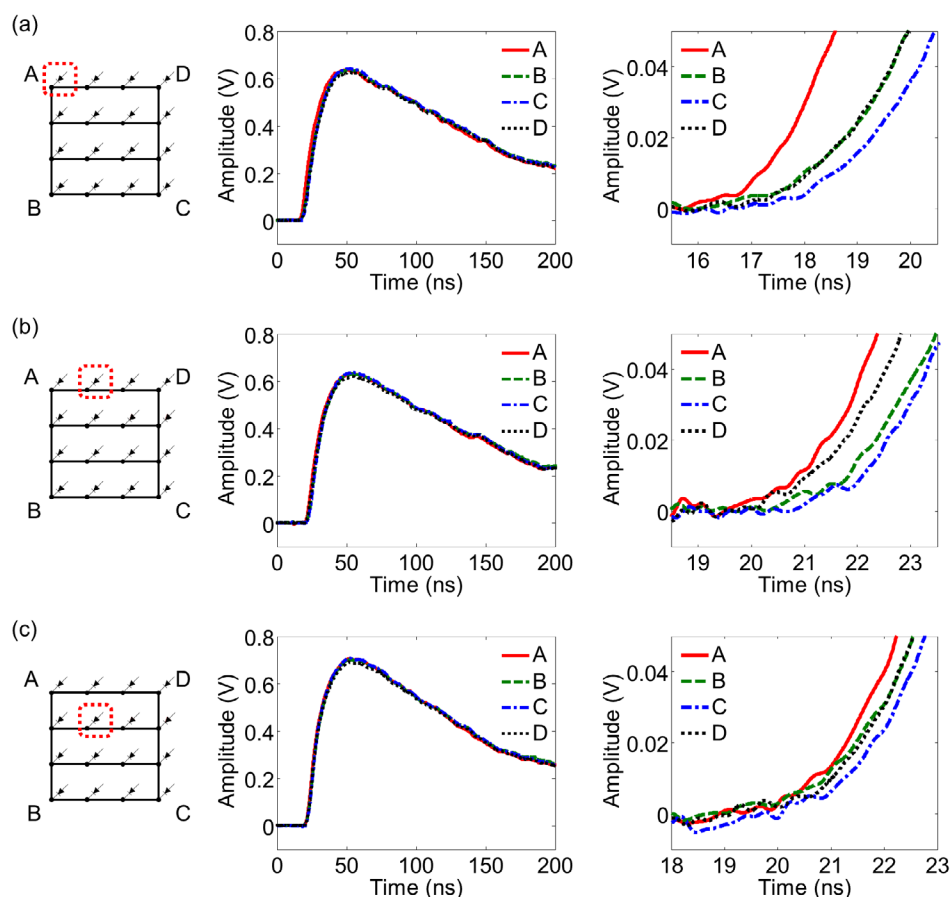


Figure 6. Waveforms obtained at the four corner readout channels. (a) Full and detailed views of waveforms for event that originated from corner location (at firing position (0, 3)). (b) Full and detailed views of waveforms for event that originated from edge location (at firing position (1, 3)). (c) Full and detailed views of waveforms for event that originated from center location (at firing position (1, 2)).

Figure 10 shows the DWRs for the flood maps shown in figure 9. LED and CFD provided the similar DWRs, and such DWRs were the largest at the 25% threshold. In addition, the DWRs increased with the overvoltage of up to 3.3 V.

Figure 11 shows the representative flood map and 1D profiles obtained using CFD with the 25% threshold at the overvoltage of 2.7 V. DWR was 9.8. The distances between the adjacent spots along the x and y directions were 367 ± 54 and 386 ± 127 ps, respectively. The FWHMs of the spots along the x and y directions were 39 ± 5 and 41 ± 4 ps, respectively.

3.1.3. Energy. Figure 12 shows the energy measurements of the LGSO/SiPM detector using the waveform sampler. Because the time pickoff method, either LED or CFD, and the threshold did not affect the energy measurements, those obtained using CFD with the 25% threshold were described. The normalized gains were not affected by both the time pickoff method and the overvoltage.

As shown in figures 12(a) and (b), the photopeak region of the total energy histogram was widened due to gain variation. Although the gain variation of the employed SiPM

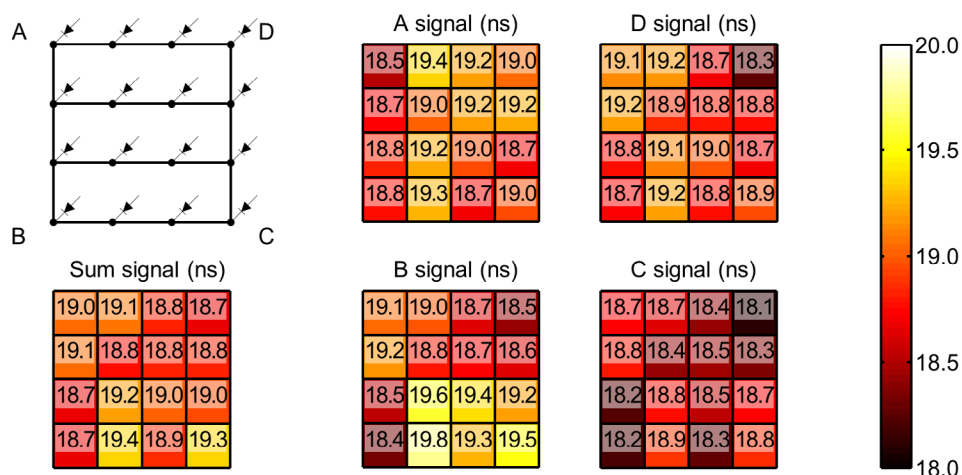


Figure 7. 10%–90% rise times of the A, B, C, D, and Sum signals for events detected at 16 SiPM channels.

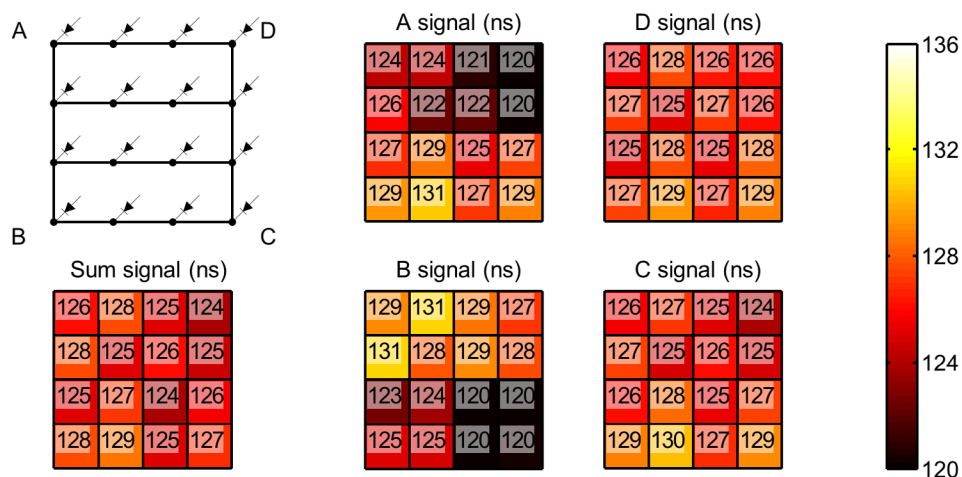


Figure 8. Decay times of the A, B, C, D, and Sum signals for events detected at 16 SiPM channels.

(S11064-050P) was negligible, the light yields of the crystals and the optical coupling were different mainly due to the slight misalignment of the crystals and the SiPM channels. The misalignment decreased the light collection efficiency of the SiPM, so that the SiPM channels located at top row of the delay grid had the lower gains than others. However, the gain variation can be corrected by crystal identification. The per-crystal energy resolutions after crystal identification were evaluated as a function of the overvoltage, as shown in figure 12(c). The error bars in figure 12(c) indicate the standard deviation of the energy resolutions of the multiplexed SiPM channels. The per-crystal energy resolutions were 9.3 ± 0.3 , 9.4 ± 0.2 , 9.3 ± 0.2 , 9.0 ± 0.2 , 8.9 ± 0.2 , and $8.7 \pm 0.2\%$ FWHM at 511 keV at the respective overvoltages from 2.1 V to 3.6 V. The energy resolution of a reference detector was 10.1% FWHM at 511 keV.

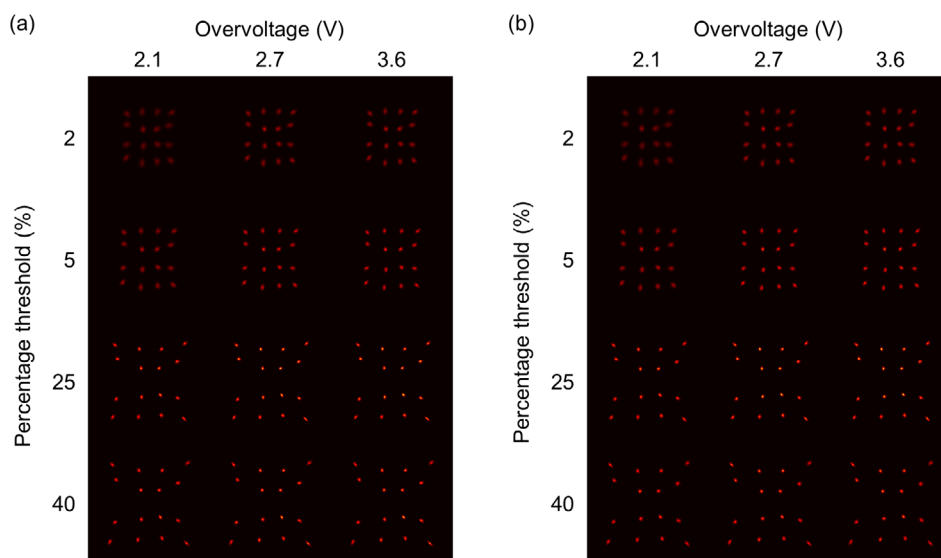


Figure 9. (a) Flood maps obtained using LED against the overvoltage and the percentage threshold. (b) Flood maps obtained using CFD against the overvoltage and the percentage threshold.

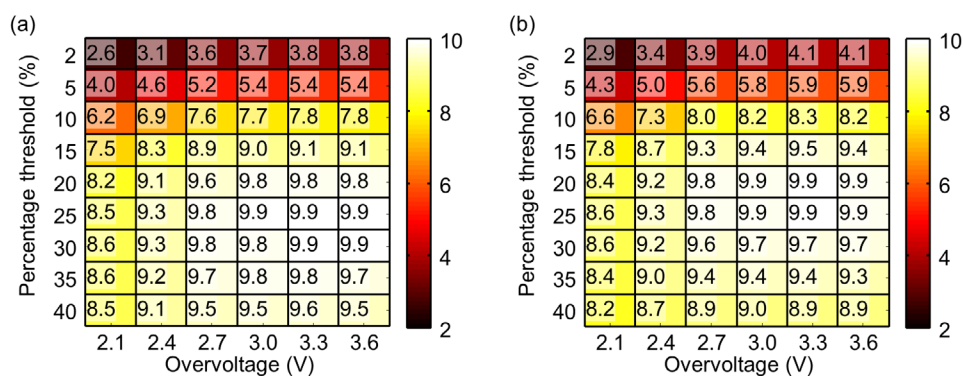


Figure 10. (a) DWRs obtained using LED against the overvoltage and the percentage threshold. (b) DWRs obtained using CFD against the overvoltage and the percentage threshold.

3.1.4. CRT. Figure 13(a) shows the time difference spectrum using $\{t_{ABCD}, \text{CFD}\}$. Figure 13(b) shows the CRTs against the overvoltage and the error bars indicate the standard deviation of CRTs of the multiplexed SiPM channels. The lowest CRTs obtained using $\{t_{ABCD}, \text{LED}\}$, $\{t_{ABCD}, \text{CFD}\}$, $\{t_{\text{Sum}}, \text{LED}\}$, and $\{t_{\text{Sum}}, \text{CFD}\}$ were 408 ± 13 , 382 ± 13 , 436 ± 19 , and 410 ± 21 ps FWHM, respectively, at an overvoltage of 2.7V. Figures 13(c)–(f) show the per-crystal CRTs measured at an overvoltage of 2.7V using $\{t_{ABCD}, \text{LED}\}$, $\{t_{ABCD}, \text{CFD}\}$, $\{t_{\text{Sum}}, \text{LED}\}$, and $\{t_{\text{Sum}}, \text{CFD}\}$, respectively.

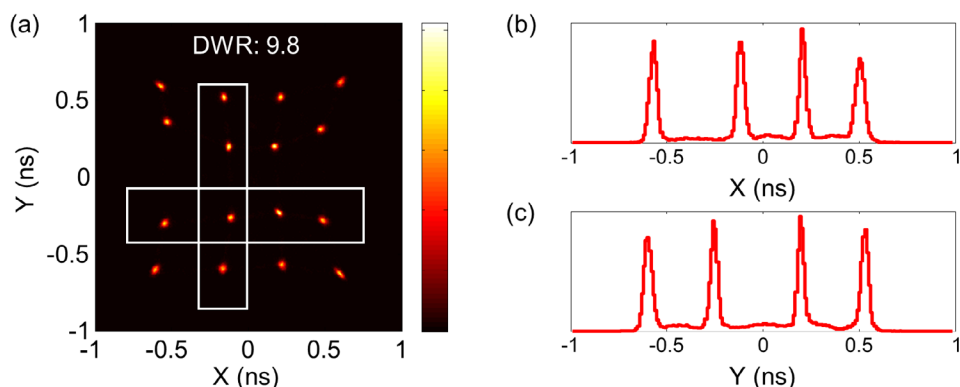


Figure 11. (a) Representative flood map obtained using CFD with the 25% threshold at the overvoltage of 2.7V. (b) 1D profile along the *x* direction. (c) 1D profile along the *y* direction.

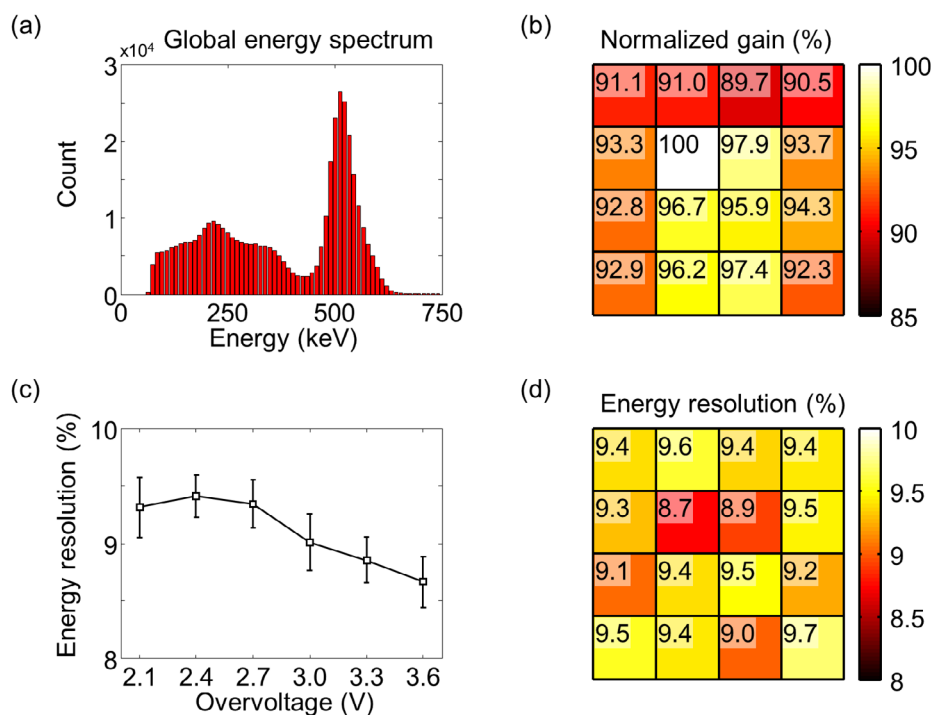


Figure 12. Energy measurements for the LGSO/SiPM detector using the waveform sampler. (a) Global energy spectrum before gain variation correction. (b) Normalized gain. (c) Per-crystal energy resolutions against the overvoltage. (d) Representative per-crystal energy resolutions obtained at an overvoltage of 2.7V.

3.2. FPGA-TDC

3.2.1. ToT and energy. Figure 14 shows the ToT measurements for the LGSO/SiPM detector using the FPGA-TDC. As shown in figure 14(a), the photopeak region was resolved well using the ToT. Figure 14(b) shows the calibration curve, and the error bars indicate the standard

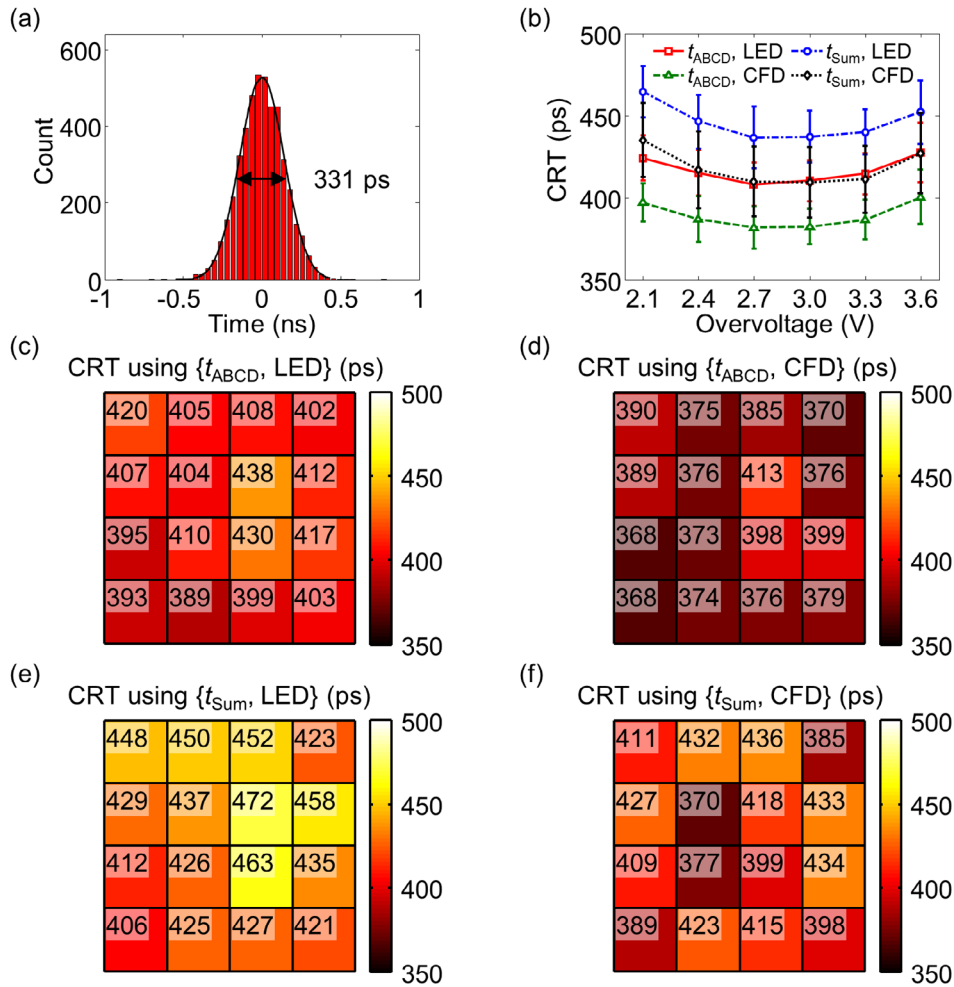


Figure 13. CRT measurements using the waveform sampler. (a) Time difference spectrum between a SiPM channel with location (1, 2) and a reference detector. Time pickoff method $\{t_{\text{ABCD, CFD}}\}$ was used for the LGSO/SiPM detector. (b) CRTs against the overvoltage. (c) Per-crystal CRTs using $\{t_{\text{ABCD, LED}}\}$. (d) Per-crystal CRTs using $\{t_{\text{ABCD, CFD}}\}$. (e) Per-crystal CRTs using $\{t_{\text{Sum, LED}}\}$. (f) Per-crystal CRTs using $\{t_{\text{Sum, CFD}}\}$. CRTs obtained at an overvoltage of 2.7V were shown.

deviation of the ToT peak positions of the multiplexed SiPM channels. Figures 14(c) and (d) show the ToT peak positions and the per-crystal energy resolutions for 511 keV photopeak measured at 16 SiPM channels, respectively. The ToT peak positions of the 16 SiPM channels had the same tendency as the normalized gains (figure 12(b)). The per-crystal energy resolution was $25.4 \pm 0.8\%$ FWHM at 511 keV.

3.2.2. Flood map. Figure 15 shows the flood map and 1D profiles while the DWR was 6.1. The distances between the adjacent spots along the x and y directions were 232 ± 25 and 295 ± 54 ps, respectively. The FWHM of the spots along the x and y directions were 42 ± 4 and 46 ± 2 ps, respectively.

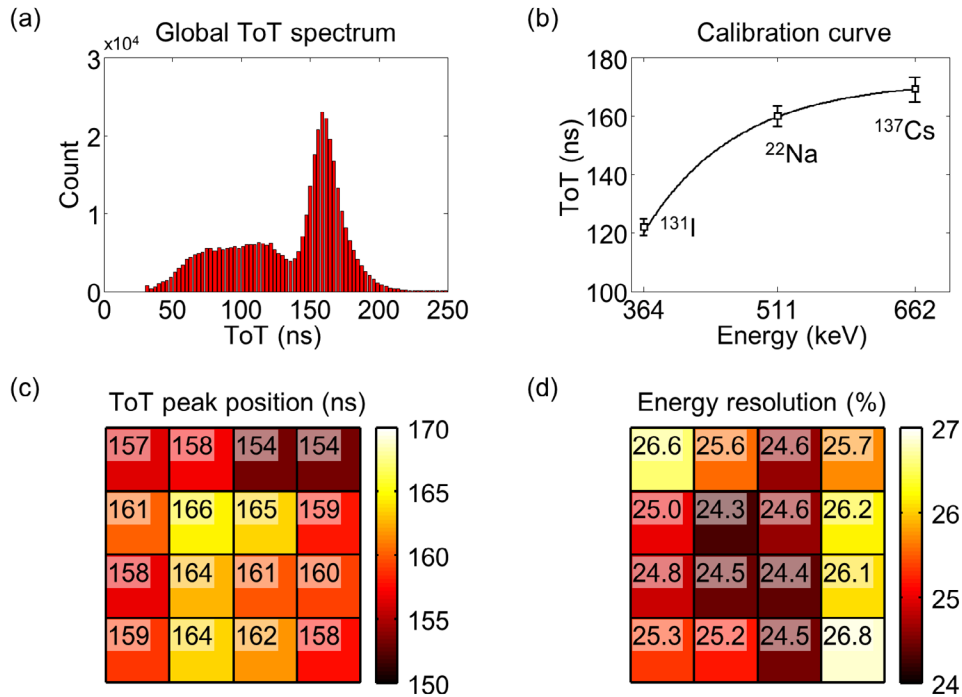


Figure 14. ToT measurements for the LGSO/SiPM detector using the FPGA-TDC. (a) Global ToT spectrum before gain variation correction. (b) ToT peak positions against energy. (c) ToT peak positions for 511 keV photopeak measured at 16 SiPM channels. (d) Per-crystal energy resolutions.

3.2.3. CRT. Figures 16(a) and (b) show the time difference spectrum using the FPGA-TDC and the per-crystal CRTs, respectively. The per-crystal CRT was 406 ± 16 ps FWHM. The CRTs acquired using the FPGA-TDC were comparable with those measured using the waveform sampler with the time pickoff method $\{t_{ABCD}, \text{LED}\}$. As with the CRTs measured using the waveform sampler, these CRTs were uniform throughout the multiplexed SiPM channels.

4. Discussion

4.1. Position

The delay grid is a planar array of microstrip traces connecting the cathodes of SiPM channels as shown in figure 2(d). The trace consists of R_0 , L_0 , G_0 , and C_0 where R_0 , L_0 , G_0 , and C_0 are the characteristic resistance, inductance, conductance, and capacitance per unit length of the trace. The time delay along the trace with the length of Δx is $\sqrt{L_0 \Delta x \times C_0 \Delta x}$ (Deutsch *et al* 1990, Montrose 2000).

A trace connecting adjacent SiPM channels has L_0 , C_0 , and Δx of 6.79×10^2 pH mm⁻¹, 4.62×10^{-2} pF mm⁻¹, and 5.24 mm, respectively, and the calculated unit delay without loading is 29 ps. This calculated unit delay is one order of magnitude lower than the measured unit delay of approximately 200–400 ps. This was because the SiPM channels were directly connected to the delay grid and the terminal capacitance C_t of the SiPM channel served as the lumped capacitive load. The capacitive loading increased the unit delay to

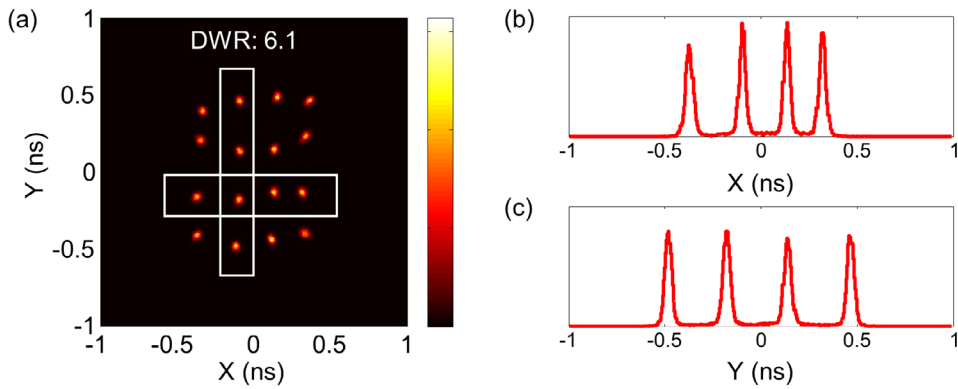


Figure 15. (a) Flood map obtained using the FPGA-TDC with the 2% threshold at an overvoltage of 2.7V. (b) 1D profile along the *x* direction. (c) 1D profile along the *y* direction.

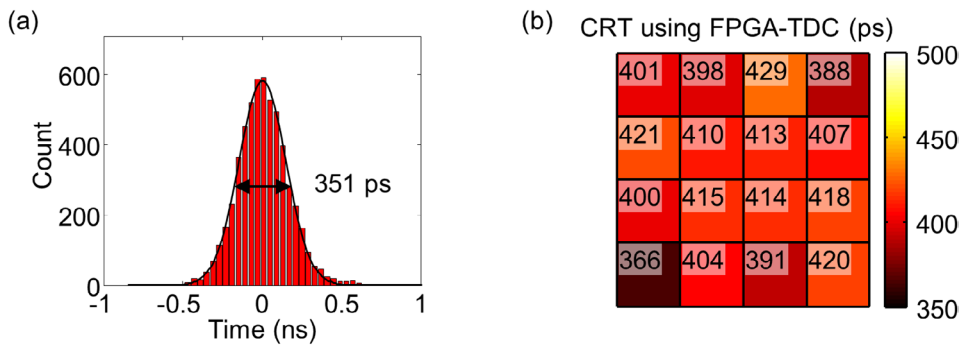


Figure 16. CRT measurements using the FPGA-TDC. (a) Time difference spectrum between a SiPM channel with location (1, 2) and a reference detector. (b) Per-crystal CRTs obtained at an overvoltage of 2.7V.

$\sqrt{L_0 \Delta x \times (C_0 \Delta x + C_t)}$ (Montrose 2000) where the C_t is the effective capacitance between the anode and the cathode of the SiPM channel and it is the junction capacitance of a single pixel C_j multiplied by the number of pixels N . The C_j , N , and C_t of the employed Hamamatsu SiPM channel are 90 fF, 3600, and 320 pF, respectively (Piatek 2014, Bieniosek *et al* 2016), and the expected unit delay including the capacitive load becomes 1068 ps obtained by calculating $\sqrt{L_0 \Delta x \times (C_0 \Delta x + C_t)}$. However, the measured unit delay was less than 1068 ps because the quenching resistor R_q of each pixel partially isolated the capacitive load as shown in figure 17.

In addition, the delay that was introduced by the capacitive loading increased with the percentage threshold, because the capacitive loading degraded the signal slope slightly and consequently the signal with less steep slope had longer transit times with the respect to the constant percentage threshold. Thus, the TDOAs and the size of the flood map increased with the percentage threshold as shown in figures 6 and 9, respectively. The increased TDOAs could provide the clearest flood maps and the highest DWRs for the 25% threshold, where the signals were the steepest. The slight pincushion distortion that appeared as the threshold increased was also due to the capacitive loading. In order to reduce the capacitive loading, the

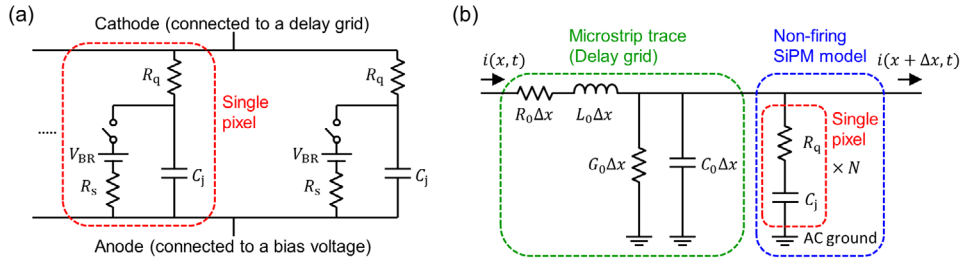


Figure 17. (a) Equivalent SiPM model. The R_q , C_j , R_s , and V_{BR} are the quenching resistor, the junction capacitance, the series resistance and the breakdown voltage of each pixel, respectively. (b) Circuit model for estimating the unit delay that is the transit time when the current from the firing SiPM channel propagates into the adjacent non-firing SiPM channel. The models in the red, green, and blue boxes indicate the single pixel of the SiPM, the microstrip trace connecting between the adjacent cathode pins, and a non-firing SiPM, respectively.

traces can be isolated from C_1 using transistors (Kim *et al* 2015) or other active elements at the expense of circuit simplicity and TDOAs.

The flood maps and the DWRs were also evaluated against the overvoltage, as shown in figures 9 and 10. The effects of overvoltage on the flood map and the DWR can be analyzed using equation (7), where σ_t , σ_v , and dv/dt are the root-mean-square (rms) time jitter, the rms noise, and the leading edge slope of a signal crossing the threshold.

$$\sigma_t = \frac{\sigma_v}{dv/dt}. \quad (7)$$

As the overvoltage increased, dv/dt also increased because the SiPM gain is proportional to the overvoltage. Although the dark noise that contributes to σ_v also increased with the overvoltage, the dark noises measured at the four corner readout channels were correlated. The covariance between the corner node arrival times reduced the effects of dark noise on decoding the position information, and thus the DWRs obtained at the overvoltage of 3.3 V were higher than those acquired at 2.7 V, where the CRTs were the lowest.

When using the 2% thresholds to decode the position information, the flood maps acquired using the waveform sampler were less clear than that obtained using the FPGA-TDC. The DWRs were 3.6 and 3.9 for the waveform sampler using LED and CFD, respectively, on the other hand, the DWR measured using the FPGA-TDC was 6.1 at the overvoltage of 2.7 V. This was because the uncertainty of the interpolation, which was conducted where the signal slope was not steep, dominantly widened the sizes of the spots in the flood map. On the other hand, the FPGA-TDC could measure the TDOAs directly with a 10 ps resolution from the digital signals discriminated by the comparators. However, the waveform sampler can apply the respective optimal thresholds for timing and position measurements in the data processing step. In addition, the flood map obtained using the FPGA-TDC can be made clearer by increasing the threshold at the four corner readout channels up to 25% and thus increasing the TDOAs and the signal slope. However, the $V_{\text{thresh,low}}$ of 2% thresholds were applied to the A, B, C, and D readout channels to improve the CRT. The details are discussed in the next section. Although the DWR acquired using the FPGA-TDC was lower than that obtained using the waveform sampler with the 25% threshold, it is worth to note that the crystals were identified using only TDC without the requirement of an ADC.

4.2. CRT

Precise CRT allows time-of-flight (TOF) PET that reduces scan times (Surti 2015, Ullah *et al* 2016) and injected doses (Surti and Karp 2015, Son *et al* 2016). The per-crystal CRTs were measured as a function of the overvoltage, as shown in figure 13. As the bias voltage increased, the CRTs followed U-shaped curves. This is because the higher bias voltage provided larger leading edge slope dv/dt , but also introduced higher dark noise that contributed to σ_v in equation (7).

CFD yielded lower CRTs than LED because CFD can eliminate the time walk (a dependence of time pickoff on the peak amplitude of the signal) and the effect of gain variation between the LGSO/SiPM channels. In addition, the per-crystal CRTs were consistent throughout the SiPM channels because the signal was not distorted considerably by a multiplexing circuit.

In addition, t_{sum} provided worse CRTs than t_{ABCD} , especially for the SiPM channels located at the corner and edge where the TDOAs were larger than for the SiPM channels located at the center of the multiplexing circuit. This is because the Sum signal was dominantly discriminated by the first arrival signal among the A, B, C, and D signals. Consequently, in equation (7), dv/dt of the Sum signal was almost identical to that of the first arrival signal, but σ_v of the Sum signal was higher than that of the respective A, B, C, and D signals because the correlated noises of the A, B, C, and D signals were added in the Sum signal. For this reason, the $V_{\text{thresh,low}}$ of 2% thresholds that correspond to early photons were applied to the four corner readout channels when an FPGA-TDC was used as the time pickoff device.

4.3. ToT

ToT is a simple method for estimating the energy information using only time measurements; however, ToT cannot be generally used after conventional multiplexing because the charge division circuit distorts the signal shape and changes the amplitude at the readout channels (Downie *et al* 2013, Goertzen *et al* 2013, Ko *et al* 2013, Olcott *et al* 2013). Contrary to the charge division circuits, the delay grid multiplexing can employ ToT after multiplexing because the signal shape and the amplitude did not change considerably by the multiplexing circuit, as shown in figure 6. In addition, it is possible to omit the summing amplifier and apply the dual-threshold ToT to one of the A, B, C, and D signals. However, because the rise and decay times of the Sum signal were more uniform than those of the A, B, C, and D signals, as shown in figures 7 and 8, ToT was obtained by applying the $V_{\text{thresh,high}}$ of 40% threshold to the Sum readout channel.

The energy resolutions obtained using the FPGA-TDC were worse than those acquired using the waveform sampler because the ToT method uses only two data points to extract the energy information, and thus is more vulnerable to noise and baseline shift than the energy integration method. However, ToT could resolve the photopeak region.

4.4. Waveform sampler versus FPGA-TDC

The waveform sampler allows the full analysis of the signals; the baseline, energy, gamma arrival time, rise time, and decay time can be obtained from a waveform. In particular, the corner node arrival times, and thus the gamma arrival time can be measured accurately because the baseline can be corrected at the signal onset on an event-by-event basis. In addition, CFD that eliminates the time walk can be applied without the complex electronics. The accurate gamma arrival time and the precise energy windowing provided better CRTs than FPGA-TDC.

Subsequently, the precise corner node arrival times obtained at the steepest slope of the signal could improve the flood-map quality. Furthermore, the depth-of-interaction measurement that involves pulse shape discrimination (Du *et al* 2009, Schmall *et al* 2015) and pulse pile-up recovery (Haselman *et al* 2012) can be applied after multiplexing thanks to minimal signal distortion by the multiplexing circuit. However, a DRS4 serves as the time stretcher, and thus requires the external ADC and FPGA that can complicate the readout circuit (Ritt *et al* 2010).

An FPGA-TDC can not only measure the fine time and the energy (using ToT), but also have design flexibility; energy discrimination, time windowing for the coincidence detection mode (Ko *et al* 2011), false event rejection, and crystal identification can be conducted using only a single FPGA where TDCs are implemented. Thus, the readout circuit can be simplified using the FPGA-TDC. In addition, the FPGA-TDC has a low data burden and can process events with a high throughput. The multi-channel FPGA-TDC that operates in parallel has a dead time of 5 ns (Won and Lee 2016), whereas the waveform sampler DT5742B requires the minimum 110 μ s digitization time for a single event. Furthermore, the FPGA-TDC has the excellent channel expandability because a TDC requires a few FPGA resources (Won and Lee 2016). The SiPM-based PET detector that consists a large number of detector channels (e.g. 64 or 256) can suffer from high multiplexing ratio that degrades the CRTs and counting performance. The high-integrity TDC allows the low multiplexing ratio (e.g. 16-to-4 or 16-to-5) using more TDC channels, and thus retaining the CRTs instead of increasing the multiplexing ratio. Thus, the delay grid multiplexing method and the FPGA-TDC are a good combination for reducing the resource and complexity of the PET detector front-end and readout electronics.

5. Conclusion

We proposed the fully time-based multiplexing and FPGA-TDC-based readout method. The crystals were clearly resolved using the time information measured at the four readout channels. In addition, the multiplexing circuit provided consistent rise times, decay times, and CRTs throughout the multiplexed SiPM channels. Furthermore, the position, the energy, and the gamma arrival time were obtained using TDCs implemented in a single FPGA, while a dual-threshold ToT method could be applied after multiplexing. The delay grid multiplexing would be useful for TOF PET measurement with compact size, low heat dissipation, and minimal usage of electronics.

Acknowledgments

This work was supported by grants from the National Research Foundation of Korea (NRF) funded by the Korean Ministry of Science, ICT and Future Planning (grant no. NRF-2014M3C7034000 and NRF-2016R1A2B3014645), and the Korea Health Technology R&D Project through the Korea Health Industry Development Institute (KHIDI), funded by the Ministry of Health & Welfare, Republic of Korea (grant no. HI14C1135).

References

- Anghinolfi F, Jarron P, Krummenacher F, Usenko E and Williams M C S 2004 NINO: an ultrafast low-power front-end amplifier discriminator for the time-of-flight detector in the ALICE experiment *IEEE Trans. Nucl. Sci.* **51** 1974–8

- Bieniosek M F, Cates J W and Levin C S 2016 Achieving fast timing performance with multiplexed SiPMs *Phys. Med. Biol.* **61** 2879–92
- Cates J W, Vinke R and Levin C S 2015 Analytical calculation of the lower bound on timing resolution for PET scintillation detectors comprising high-aspect-ratio crystal elements *Phys. Med. Biol.* **60** 5141–61
- Deutsch A et al 1990 High-speed signal propagation on lossy transmission lines *IBM J. Res. Dev.* **34** 601–15
- Downie E, Yang X and Peng H 2013 Investigation of analog charge multiplexing schemes for SiPM based PET block detectors *Phys. Med. Biol.* **58** 3943–64
- Du J, Schmall J P, Yang Y, Di K, Dokhale P A, Shah K S and Cherry S R 2013 A simple capacitive charge-division readout for position-sensitive solid-state photomultiplier arrays *IEEE Trans. Nucl. Sci.* **60** 3188–97
- Du H, Yang Y, Glodo J, Wu Y, Shah K and Cherry S R 2009 Continuous depth-of-interaction encoding using phosphor-coated scintillators *Phys. Med. Biol.* **54** 1757–71
- Goertzen A L et al 2013 Design and performance of a resistor multiplexing readout circuit for a SiPM detector *IEEE Trans. Nucl. Sci.* **60** 1541–9
- Grant A M and Levin C S 2014 A new dual threshold time-over-threshold circuit for fast timing in PET *Phys. Med. Biol.* **59** 3421–30
- Harion T, Briggel K, Chen H, Fischer P, Gil A, Kiworra V, Ritzert M, Schultz-Coulon H-C, Shen W and Stankova V 2014 STiC—a mixed mode silicon photomultiplier readout ASIC for time-of-flight applications *J. Instrum.* **9** C02003
- Haselman M D, Pasko J, Hauck S, Lewellen T K and Miyaoka R S 2012 FPGA-based pulse pile-up correction with energy and timing recovery *IEEE Trans. Nucl. Sci.* **59** 1823–30
- Hong S J, Kang H G, Ko G B, Song I C, Rhee J-T and Lee J S 2012 SiPM-PET with a short optical fiber bundle for simultaneous PET-MR imaging *Phys. Med. Biol.* **57** 3869–83
- Ito M, Lee J P and Lee J S 2013 Timing performance study of new fast PMTs with LYSO for time-of-flight PET *IEEE Trans. Nucl. Sci.* **60** 30–7
- Jung J H, Choi Y and Im K C 2016 PET/MRI: technical challenges and recent advances *Nucl. Med. Mol. Imaging* **50** 3–12
- Kim H, Chen C-T, Eclow N, Ronzhin A, Murat P, Ramberg E, Los S, Wyrwicz A M, Li L and Kao C-M 2015 A feasibility study of a PET/MRI insert detector using strip-line and waveform sampling data acquisition *Nucl. Instrum. Methods A* **784** 557–64
- Kim H, Chen C-T, Frisch H, Tang F and Kao C-M 2012 A prototype TOF PET detector module using a micro-channel plate photomultiplier tube with waveform sampling *Nucl. Instrum. Methods A* **662** 26–32
- Kim C L, McDaniel D L and Ganin A 2011 Time-of-flight PET detector based on multi-pixel photon counter and its challenges *IEEE Trans. Nucl. Sci.* **58** 3–8
- Ko G B, Kim K Y, Yoon H S, Lee M S, Son J-W, Im H-J and Lee J S 2016a Evaluation of a silicon photomultiplier PET insert for simultaneous PET and MR imaging *Med. Phys.* **43** 72–83
- Ko G B, Yoon H S, Kim K Y, Lee M S, Yang B Y, Jeong J M, Lee D S, Song I C, Kim S-k, Kim D and Lee J S 2016b Simultaneous multiparametric PET/MRI with silicon photomultiplier PET and ultra-high-field MRI for small-animal imaging *J. Nucl. Med.* **57** 1309–15
- Ko G B and Lee J S 2015 Performance characterization of high quantum efficiency metal package photomultiplier tubes for time-of-flight and high-resolution PET applications *Med. Phys.* **42** 510–20
- Ko G B, Yoon H S, Kwon S I, Hong S J, Lee D S and Lee J S 2011 Development of FPGA-based coincidence units with veto function *Biomed. Eng. Lett.* **1** 27–31
- Ko G B, Yoon H S, Kwon S I, Lee C M, Ito M, Hong S J, Lee D S and Lee J S 2013 Development of a front-end analog circuit for multi-channel SiPM readout and performance verification for various PET detector designs *Nucl. Instrum. Methods A* **703** 38–44
- Kwon S I and Lee J S 2014 Signal encoding method for a time-of-flight PET detector using a silicon photomultiplier array *Nucl. Instrum. Methods A* **761** 39–45
- Lee J S and Hong S J 2010 Geiger-mode avalanche photodiodes for PET/MRI *Electronics for Radiation Detection* ed K Iniewski (Boca Raton, FL: CRC Press) pp 179–200
- Lee M S and Lee J S 2015 Depth-of-interaction measurement in a single-layer crystal array with a single-ended readout using digital silicon photomultiplier *Phys. Med. Biol.* **60** 6495–514
- Montrose M I 2000 *Printed Circuit Board Design Techniques for EMC Compliance: a Handbook for Designers* 2nd edn (New York: Wiley)

- Nemallapudi M V, Gundacker S, Lecoq P, Auffray E, Ferri A, Gola A and Piemonte C 2015 Sub-100 ps coincidence time resolution for positron emission tomography with LSO:Ce codoped with Ca *Phys. Med. Biol.* **60** 4635–49
- Olcott P D, Glover G and Levin C S 2013 Cross-strip multiplexed electro-optical coupled scintillation detector for integrated PET/MRI *IEEE Trans. Nucl. Sci.* **60** 3198–204
- Olcott P, Kim E, Hong K, Lee B J, Grant A M, Chang C-M, Glover G and Levin C S 2015 Prototype positron emission tomography insert with electro-optical signal transmission for simultaneous operation with MRI *Phys. Med. Biol.* **60** 3459–78
- Piatek S 2014 *Measuring the Electrical and Optical Properties of an MPPC* Hamamatsu Corporation & New Jersey Institute of Technology (www.hamamatsu.com/us/en/community/optical_sensors/articles/measuring_characteristics_of_mppc/index.html) (Accessed: 1 September 2016)
- Popov V, Majewski S and Welch B L 2006 A novel readout concept for multianode photomultiplier tubes with pad matrix anode layout *Nucl. Instrum. Methods A* **567** 319–22
- Ritt S, Dinapoli R and Hartmann U 2010 Application of the DRS chip for fast waveform digitizing *Nucl. Instrum. Methods A* **623** 486–8
- Roncali E and Cherry S R 2011 Application of silicon photomultipliers to positron emission tomography *Ann. Biomed. Eng.* **39** 1358–77
- Schaart D R, Seifert S, Vinke R, van Dam H T, Dendooven P, Löhner H and Beekman F J 2010 LaBr₃:Ce and SiPMs for time-of-flight PET: achieving 100 ps coincidence resolving time *Phys. Med. Biol.* **55** N179–89
- Schmall J P, Surti S and Karp J S 2015 Characterization of stacked-crystal PET detector designs for measurement of both TOF and DOI *Phys. Med. Biol.* **60** 3549–65
- Shimazoe K, Takahashi H, Shi B, Furumiya T, Ooi J, Kumazawa Y and Murayama H 2010 Novel front-end pulse processing scheme for PET system based on pulse width modulation and pulse train method *IEEE Trans. Nucl. Sci.* **57** 782–6
- Siegel S, Silverman R W, Shao Y and Cherry S R 1996 Simple charge division readouts for imaging scintillator arrays using a multi-channel PMT *IEEE Trans. Nucl. Sci.* **43** 1634–41
- Son J-W, Ko G B, Won J Y, Yoon H S and Lee J S 2016 Development and performance evaluation of a time-of-flight positron emission tomography detector based on a high-quantum-efficiency multi-anode photomultiplier tube *IEEE Trans. Nucl. Sci.* **63** 44–51
- Stolin A V, Majewski S, Jaliparthi G, Raylman R R and Proffitt J 2014 Evaluation of imaging modules based on SensL array SB-8 for nuclear medicine applications *IEEE Trans. Nucl. Sci.* **61** 2433–8
- Surti S 2015 Update on time-of-flight PET imaging *J. Nucl. Med.* **56** 98–105
- Surti S and Karp J S 2015 Impact of detector design on imaging performance of a long axial field-of-view, whole-body PET scanner *Phys. Med. Biol.* **60** 5343–58
- Ullah M N, Pratiwi E, Cheon J, Choi H and Yeom J Y 2016 Instrumentation for time-of-flight positron emission tomography *Nucl. Med. Mol. Imaging* **50** 112–22
- Wehrl H F, Sauter A W, Divine M R and Pichler B J 2015 Combined PET/MR: a technology becomes mature *J. Nucl. Med.* **56** 165–8
- Weissler B *et al* 2015 A digital preclinical PET/MRI insert and initial results *IEEE Trans. Med. Imaging* **34** 2258–70
- Won J Y, Kwon S I, Yoon H S, Ko G B, Son J-W and Lee J S 2016 Dual-phase tapped-delay-line time-to-digital converter with on-the-fly calibration implemented in 40 nm FPGA *IEEE Trans. Biomed. Circuits Syst.* **10** 231–42
- Won J Y and Lee J S 2016 Time-to-digital converter using a tuned-delay line evaluated in 28-, 40-, and 45-nm FPGAs *IEEE Trans. Instrum. Meas.* **65** 1678–89
- Yamamoto S, Watabe T, Watabe H, Aoki M, Sugiyama E, Imaizumi M, Kanai Y, Shimosegawa E and Hatazawa J 2012 Simultaneous imaging using Si-PM-based PET and MRI for development of an integrated PET/MRI system *Phys. Med. Biol.* **57** N1–13
- Yeom J Y, Vinke R, Spanoudaki V C, Hong K J and Levin C S 2013a Readout electronics and data acquisition of a positron emission tomography time-of-flight detector module with waveform digitizer *IEEE Trans. Nucl. Sci.* **60** 3735–41
- Yeom J Y, Vinke R and Levin C S 2013b Optimizing timing performance of silicon photomultiplier-based scintillation detectors *Phys. Med. Biol.* **58** 1207–20
- Yoon H S, Ko G B, Kwon S I, Lee C M, Ito M, Song I C, Lee D S, Hong S J and Lee J S 2012 Initial results of simultaneous PET/MRI experiments with an MRI-compatible silicon photomultiplier PET scanner *J. Nucl. Med.* **53** 608–14